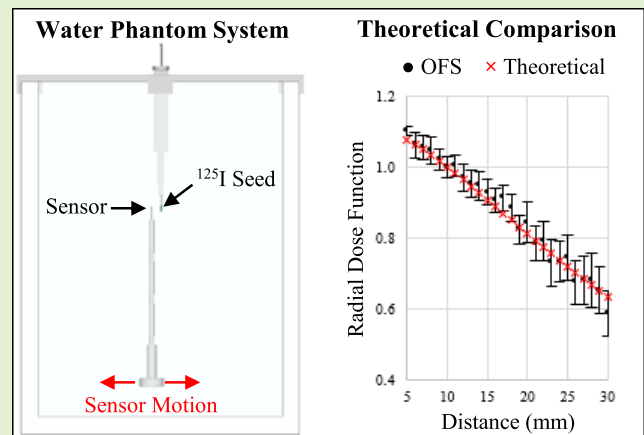


Water Phantom Characterization of a Novel Optical Fiber Sensor for LDR Brachytherapy

Michael Martyn¹, Member, IEEE, Wern Kam², Member, IEEE, Peter Woulfe, Member, IEEE, and Sinead O'Keefe³, Member, IEEE

Abstract—This work considers the feasibility of using a novel optical fiber-based sensor, employing a terbium-doped gadolinium oxysulfide ($Gd_2O_2S:Tb$) inorganic scintillator, as a real-time in vivo dosimetry solution for applications in low-dose-rate (LDR) prostate brachytherapy (BT). This study specifically considers the influence of scintillator geometry (hemisphere tip versus cylindrical cavity), polymethyl methacrylate (PMMA) fiber core diameter (0.5 versus 1.0 mm), and sensor housing material (stainless steel versus plastic) on the measured scintillation signal. Characterization measurements were performed using a silicon photon-multiplier (SiPM) detector and a commercial water phantom system, integrated with custom 3-D printed components to allow for precise positioning of the LDR BT radiation source with respect to the optical fiber sensor (OFS). Significant differences in the rate of fall-off in the scintillation signal, with distance from the source, were observed between the different scintillator geometries considered. The hemisphere tip geometry was shown to be the most accurate, tracking with the expected fall-off in dose-rate, within measurement uncertainty. Reducing the fiber core diameter from 1.0 to 0.5 mm resulted in a sixfold reduction in the detected scintillation signal. A further 57% reduction was observed when housing the 0.5-mm fiber within a stainless steel LDR BT needle applicator. Initial results demonstrate the feasibility of employing an OFS, for applications in LDR BT, given the excellent agreement of measurements with theoretical expectations. Furthermore, a calibration process has been described for converting the detected scintillation signal into absorbed dose/dose rate, using our water phantom-based experimental setup.

Index Terms—Brachytherapy (BT), in vivo dosimetry, optical fiber, radiation dosimetry, silicon photomultiplier.



some form of RT, after their cancer diagnosis [1], [2], [3]. RT can be divided into external beam RT (EBRT), referring to the use of a linear accelerator to deliver radiation from outside the patient's body, or brachytherapy (BT), referring to the use of radioactive sources that are implanted within, or in close proximity to, the critical target. BT can be divided into categories based on the dose rate of the employed radioactive source, with low-dose-rate (LDR) and high-dose-rate (HDR) BT employing sources with dose rates of <2 and >12 Gy/h, respectively [4]. BT treatments can also be categorized based on the implantation technique employed (i.e., permanent implantation versus temporary implantation). This work focuses on LDR prostate BT, employing a permanent implantation technique, and iodine 125 (^{125}I) as the LDR BT source [5], [6]. Due to the steep dose gradients associated with LDR BT sources, precise positioning of the source is crucial to ensure both target coverage and minimization of the dose to uninvolved tissues and organs at risk (e.g., bladder, urethra, and rectum). Currently, source positioning during treatment delivery relies on transrectal ultrasound imaging (TRUS), which can be challenging due to the low echogenic properties

I. INTRODUCTION

RADIODTHERAPY (RT) is commonly employed for the treatment of cancer, with 50%–60% of patients requiring

Manuscript received 24 October 2022; revised 23 November 2022; accepted 23 November 2022. Date of publication 2 December 2022; date of current version 12 January 2023. This work was supported by the European Union's Horizon 2020 Research and Innovation Programme under Grant 871324. The work of Sinead O'Keefe was supported by the Royal Society and Science Foundation Ireland through the Royal Society-SFI University Research Fellowship under Grant UF150618. The associate editor coordinating the review of this article and approving it for publication was Prof. Carlos Marques. (Corresponding author: Michael Martyn.)

Michael Martyn is with the Department of Medical Physics, Blackrock Health Galway Clinic, Galway, H91 HHT0 Ireland, and also with the Physics Unit, School of Natural Sciences, University of Galway, Galway, H91 TK33 Ireland (e-mail: michael.martyn@galwayclinic.com).

Wern Kam and Sinead O'Keefe are with the Optical Fiber Sensors Research Centre and the Health Research Institute, University of Limerick, Limerick, V94 T9PX Ireland.

Peter Woulfe is with the Department of Medical Physics, Blackrock Health Galway Clinic, Galway, H91 HHT0 Ireland, and also with the Optical Fiber Sensors Research Centre, University of Limerick, Limerick, V94 T9PX Ireland.

Digital Object Identifier 10.1109/JSEN.2022.3225007

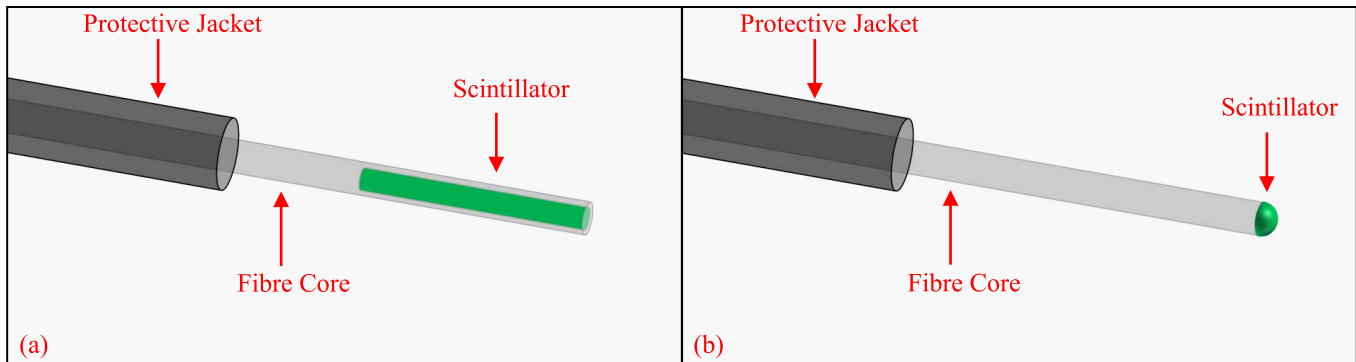


Fig. 1. OFS with (a) cylindrical cavity and (b) hemisphere tip scintillator geometry.

of radioactive ^{125}I sources (typically referred to as seeds) [7]. The final verification of source positions is therefore typically performed using a post-implantation computed tomography (CT) image and/or magnetic resonance imaging (MRI) [8]. Post-implantation CT images are typically acquired on the day of treatment as an initial indication of implant quality, and 30 days after treatment, at which point swelling of the prostate has subsided providing a better estimate of relevant dosimetric metrics, in terms of target coverage (D90, V100, V150, and so on) and OAR constraints (D2cc Rectum, D30 Urethra, and so on) [6].

Post-implantation MRI imaging, in combination with CT imaging, has also been considered as a method for improving soft tissue delineation [9]. Post-implantation CT/MRI imaging, however, does not represent real-time independent monitoring of the actual dose delivered to the patient and, as such, creates an environment where errors may go undetected during implantation. Furthermore, any issues that are identified using post-implantation CT/MRI may be difficult for clinicians to address, if at all possible.

The Horizon 2020 funded ORIGIN Project (Grant Agreement ID: 871324) aims to overcome these challenges, by providing a real-time in vivo dosimetry solution for applications in LDR prostate BT. This will be achieved through the development of a novel optical fiber-based sensor system, employing a terbium-doped gadolinium oxysulfide ($\text{Gd}_2\text{O}_2\text{S:Tb}$) inorganic scintillator. Optical fiber-based sensors have the small size required for insertion into BT needle applicators/catheters, allowing for potential in vivo measurements during a procedure. Previous work by Woulfe et al. [10] has reported initial results demonstrating the potential of $\text{Gd}_2\text{O}_2\text{S:Tb}$ as a scintillator for applications in LDR prostate BT.

This study considers the characterization of the optical fiber sensor (OFS) design previously described [10], as well as additional sensor designs varying both the scintillator geometry at the tip of the sensor and the polymethyl methacrylate (PMMA) fiber core diameter. Characterization was performed using a commercial water phantom system integrated with custom 3-D printed components, allowing for a more precise evaluation of sensor performance. Therriault-Proulx et al. [11] have previously considered validation of a plastic scintillation detector for applications in LDR BT using a water phantom setup, with a reported accuracy of ± 1.0 mm. This work,

however, considers a water phantom system employing a mechanical stage with an improved accuracy of ± 0.1 mm and provides a detailed description of the integrated novel 3-D printed components. Finally, the influence of housing the sensor in a clinically relevant stainless steel (CP Medical Inc., GA, USA) LDR BT needle applicator was considered. To the best of the authors' knowledge, we are the first group to characterize inorganic scintillation detectors, for applications in LDR BT, in this way.

II. METHODS AND MATERIALS

A. Optical Fiber Sensors

1) *Scintillator Powder*: $\text{Gd}_2\text{O}_2\text{S:Tb}$ powder was considered as the scintillator in this work. It was obtained from Phosphor Technology Ltd., U.K. (Type UKL65/F-R1), has a density of ~ 7.34 g/cm³ and a median particle size of 3.5 μm [12].

When exposed to ionizing radiation, $\text{Gd}_2\text{O}_2\text{S:Tb}$ produces scintillation light, characterized by a primary peak wavelength of 545 nm and a decay time of ~ 600 μs [13], implying that each primary gamma interaction within the scintillator powder produces a series of single photons, requiring the use of detectors with single-photon detection capabilities.

2) *Scintillator Geometry*: Two scintillator geometries were considered to investigate their influence on measurement accuracy: 1) a cylindrical cavity and 2) a hemisphere tip (see Fig. 1(a) and (b), respectively). For the cylindrical cavity, precision drilling of the PMMA fiber core tip was performed to create a 0.7-mm-diameter cavity; two different cavity depths of 5 and 7 mm were considered. The cavities were filled with scintillator powder and sealed at the tip with Henkel Loctite Hysol medical device epoxy. A hemisphere tip geometry was also considered, where the diameter of the hemisphere was chosen to be 1.0 mm. The tip itself consisted of a mixture of scintillator powder and Norland optical adhesive (NOA) 61 epoxy (3:2 ratio). The hemisphere tip was affixed to the PMMA fiber core and cured using an externally applied ultraviolet (UV) lamp.

3) *PMMA Fiber Core Diameter*: Measurements were performed with sensors fabricated using a PMMA fiber core diameter of 1.0 mm and a total outer diameter of 2.2 mm, including the protective jacket (Mitsubishi Chemical Group, Super Eska, SH4001). Measurements were also performed with a sensor fabricated using a PMMA fiber core diameter

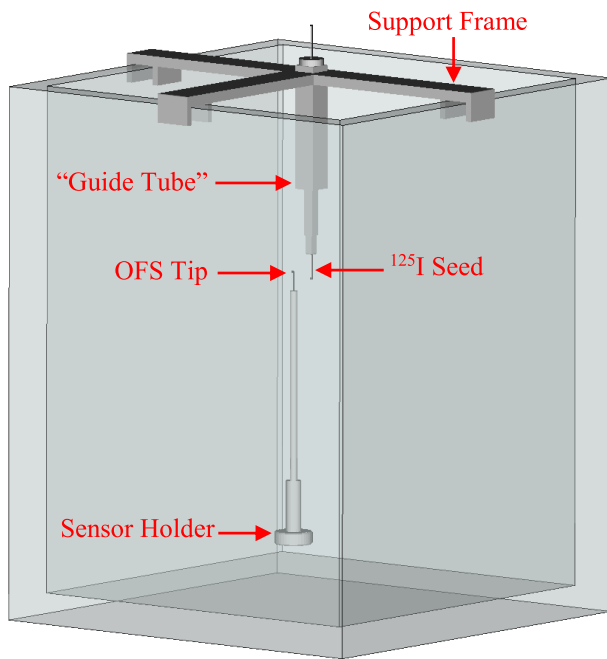


Fig. 2. Water phantom experimental setup employed for acquiring measurement data. The ^{125}I seed (within a plastic needle) and the sensor tip (also within a plastic needle) are labeled, as are the 3-D printed components. See the Appendix for schematics, including dimensions, of 3-D printed components.

of 0.5 mm (hemisphere tip scintillator geometry only) and a total outer diameter of 1.0 mm, including the protective jacket (Asahi Kasei, DC-500). With a total outer diameter of 1.0 mm, this sensor has the potential to be inserted into the clinically employed 18 gauge needle applicator, which has an inner diameter of ~ 1.0 mm.

B. Water Phantom System

All of the measurement data presented in this study were acquired using the PTW MP3-XS water phantom system (PTW, Freiburg, Germany). The use of a water phantom, filled with sterile water, allows for clinically relevant measurements to be obtained in a standardized, reproducible, and dosimetrically accurate environment. A key feature of the water phantom system is the 3-D stainless steel mechanical stage capable of moving in increments of 0.1 mm, therefore allowing for high-resolution sampling of the steep dose gradients associated with BT sources. The accuracy of the mechanical stage is also defined as being ± 0.1 mm by the manufacturer [14]. The water phantom system also has an accompanying control software, MEPHYSTO mc², which allows the user to design custom “task lists,” enabling the design of measurement schemes, automating data acquisition.

To achieve the goal of employing the water phantom system described, for LDR BT measurements, a method for positioning the radiation source relative to the OFS had to be developed. This was achieved through the design of custom 3-D printed components, which were integrated with the PTW water phantom system (see Fig. 2). PolyJet¹ material (model

MED610), which is a polymer-like material with a density of 1.17–1.18 g/cm³, was employed for all 3-D printing. The 3-D printer employed was the Stratasys Objet Connex500 with a printing accuracy of ~ 64 μm .

Three main components were printed: 1) a support frame; 2) a source holder; and 3) a sensor holder. The support frame consists of a T-junction top support, which slots onto the top of the water phantom. A 10-cm-long “guide tube” extends from the support frame into the water phantom; this feature was designed to reduce setup uncertainty by constraining the alignment of the source holder, helping to ensure that the source is positioned in a parallel orientation. The T-junction design also ensures that the source holder is delivered to the same point within the water phantom for each setup. A 3-D printed source holder was also designed for housing a plastic needle (obtained from Eckert & Ziegler Bebig GmbH, Berlin, Germany, Product Ref: LLA200-KB) within which the ^{125}I seed is placed. The 3-D printed source holder component once again acts to constrain the alignment of the plastic needle, through which the source is inserted, and in this way ensures that the source is positioned parallel to the sensor. The cuboid design of both the guide tube and the source holder component eliminates rotational variations between experiments (i.e., the source holder does not rotate within the guide tube). The plastic needle protrudes (~ 10 mm) from the bottom of the 3-D printed cuboid section to allow for more precise positioning and alignment of the ^{125}I source with the sensor. Finally, the 3-D printed OFS holder is designed such that it slots into the PTW TRUFIX “Markus Electron Chamber” holder. It can therefore be mounted on the mechanical stage of the water phantom, allowing for precise measurements to be performed. Once again, the guide tube design feature is employed to enable accurate setup and positioning of the sensor with respect to the source. Variations of this component were designed to allow for the sensor to be housed within a plastic needle (obtained from Eckert & Ziegler Bebig GmbH, Product Ref: LLA250-K15) or a stainless-steel BT needle (obtained from CP Medical Inc., Product Ref: CPPS-MN-1821-5), with only the diameter of the 3-D printed channel changing to match that of the specific needle employed. The specific needle housing the sensor protrudes (~ 10 mm) from the guide tube component to allow for more precise positioning and alignment of the sensor with the ^{125}I source.

C. Photon Counting Detector System

The photon counting detector system employed in this work is provided as part of the CAEN SP5600E Educational Photon Kit [15]. The components employed were the CAEN SP5600 power supply and amplification unit (PSAU), the CAEN DT5720A desktop digitizer (required only for activation of the CAEN control software), and a Hamamatsu silicon photomultiplier (SiPM) [model S13360-1350CS]. This SiPM has an active area of 1.3×1.3 mm² and a pixel pitch of 50 μm . The SiPM holder, which mounts onto the front end of the PSAU, has an embedded temperature feedback sensor allowing for gain compensation. The OFS is interfaced to the SiPM via an FC terminated connection. Furthermore, the PSAU and digitizer are interfaced to the laptop via USB 2.0 connections,

¹Trademarked.

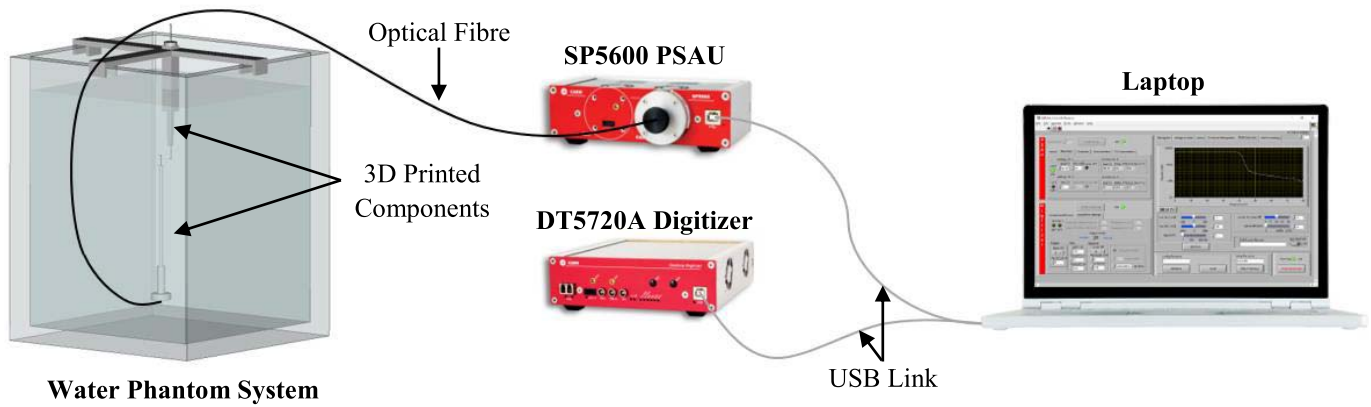


Fig. 3. Schematic of the experimental setup.

TABLE I
CONTROL SOFTWARE DATA ACQUISITION PARAMETERS

Parameter	Value
Operating Bias Voltage (V)	55.59
Gain (dB)	37
Threshold Voltage (mV)	-15
Gate-Width (ms)	10
# of Points for Mean	10

allowing for readout and analysis of measurement data. Fig. 3 shows the full schematic of the experimental setup employed, incorporating the water phantom system, the custom 3-D printed components, and the photon counting detector system.

D. Measurement Procedure

For the water phantom setup shown in Figs. 2 and 3, the ^{125}I seed is surrounded with ≥ 10 cm of sterile water in all directions, ensuring consistent and accurate scattering conditions. Both the ^{125}I seed and sensor were also ≥ 10 cm from the metal components of the water phantom system at all times. Initially, the sensor and the radiation source are positioned parallel to one another, with their centers aligned, defining a preliminary “null point” (i.e., the origin of the coordinate system). This in turn defines the position of the sensor relative to the ^{125}I seed (note: the sensor is positioned 10 mm from the source when defining the “null point”). This null point definition is then confirmed radiologically, that is to say, when the sensor and the source are correctly aligned, the scintillation signal detected at equal distances, on opposing sides of the source, should be equivalent. This is due to the cylindrically symmetrical dose distribution about the source and symmetrical geometries of the scintillators (cylindrical cavities and hemisphere tip). Fine-tuning of the null point, in 0.1-mm increments, is performed until this condition is met, within measurement uncertainty.

Within the CAEN Control Software, the user defines a number of data acquisition parameters (see Table I), including the

SiPM bias voltage (defined by Hamamatsu as the breakdown voltage +3 V), amplifier gain, threshold voltage above which an “event” is counted, and various counting parameters [e.g., the gate width and the number of data points averaged when calculating the photon counting rate (PCR)]. The measurement acquisition process has been automated through the use of the MEPHYSTO mc² control software, allowing the user to define the position and duration of each measurement. The dark count rate (DCR), which is the signal generated within the SiPM in the absence of a scintillation signal, was averaged over 30 s and performed off-axis > 10 cm from the source, an AgX100 ^{125}I seed, provided by Theragenics Corporation (GA, USA), with an activity of approximately 0.336 mCi. The PCR, which is the signal generated within the SiPM in excess of the DCR, due to the presence of a scintillation signal, was similarly averaged over 30 s. For all of the data presented in this study, consistent ambient conditions (e.g., lighting and room temperature) were maintained. Note that measurements were performed in a dark room, with the sensors housed in needles that were opaque to visible light.

Measurement files generated using the CAEN detector system were analyzed using Microsoft Excel. Data analysis involved: 1) segmentation of the raw dataset file consisting of thousands of raw count values, so as to assign each data point to the relevant measurement position; 2) subtraction of the mean DCR value from the raw counts to provide a measure of the PCR; and 3) calculation of the mean PCR signal and the standard deviation of the PCR signal, at each position.

E. Error Analysis

The random noise component, of the overall measurement uncertainty, is defined as the standard error of the mean measurement signal ($\sigma_{\bar{\mu}_i}$). Multiply $\sigma_{\bar{\mu}_i}$ by 3 to give an approximate coverage of 99.7%.

There is, however, also a positional uncertainty component, which is given by the mechanical stage accuracy, defined by the manufacturer as ± 0.1 mm. To understand how this positional uncertainty manifests as an uncertainty in the mean measurement signal, at a particular distance from the ^{125}I source, we must first understand how the expected dose rate varies as a function of distance from the ^{125}I source. If we

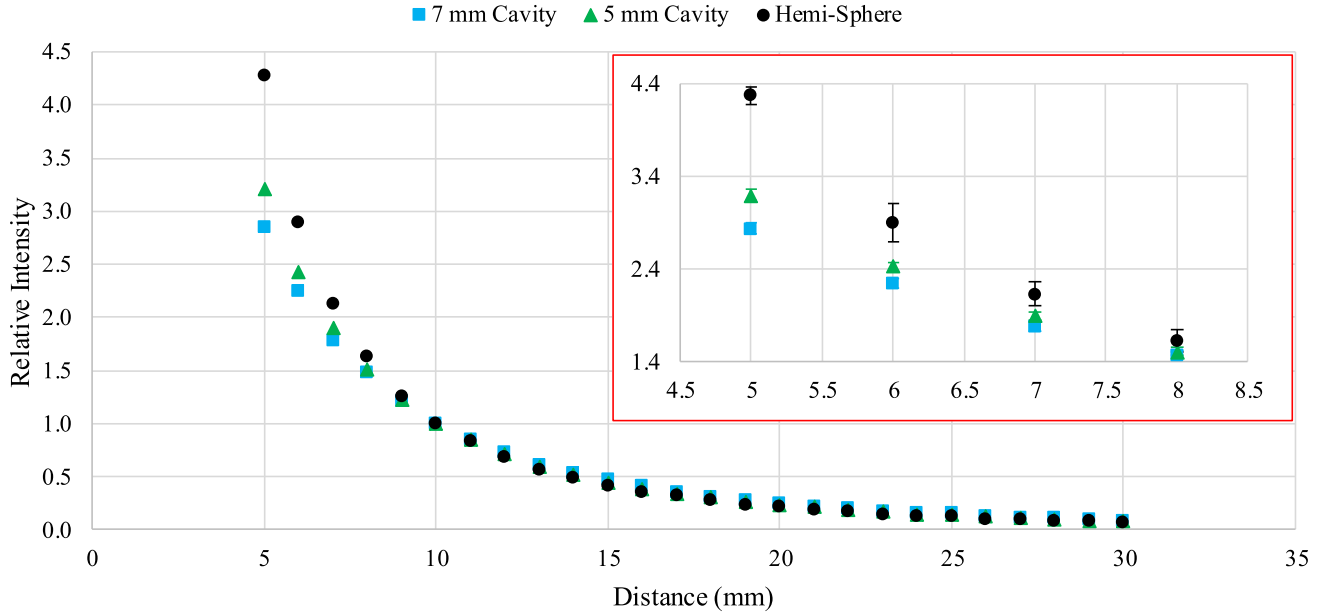


Fig. 4. Relative comparison of the fall-off in PCR along the transverse axis as a function of distance from the source, for each of the scintillator geometries considered in this work (normalized at 10 mm). An inset of the data from 5 to 8 mm is included on the right-hand side of the graph, rescaled for clarity.

begin by considering the American Association of Physicists in Medicine (AAPM) Task Group No. 43 Report [16], [17], the dose rate can be calculated at some point of interest $P(r, \theta)$, where r is the distance from the center of the source to the point of interest and θ is the angle with respect to the long axis of the source

$$\dot{D}(r, \theta) = S_K \Lambda \frac{G(r, \theta)}{G(r_0, \theta_0)} g(r) F(r, \theta). \quad (1)$$

Here, S_K and Λ are constants, which describe the air-kerma strength of the source and the dose rate constant, respectively. $F(r, \theta)$ describes the anisotropy function, which is equal to unity in this work since all measurements were performed at $\theta = \pi/2$ radians, with respect to the source. $G(r, \theta)$ is the geometry factor and $g(r)$ is the radial dose function.

For the purpose of this work, the constants S_K and Λ , and the function $F(r, \theta)$, do not influence the rate at which the calculated dose rate varies with distance from the source. We, therefore, focus on $G(r, \theta)$ and $g(r)$. Employing the line source approximation, the geometry factor is calculated as

$$G(r, \theta) = \frac{\beta}{L \cdot r \cdot \sin \theta} \quad (2)$$

where L is the source active length (3.5 mm for the AgX100 ^{125}I seed) and β is the angle subtended by the source with respect to the point of interest.

The radial dose function is described by a modified polynomial [18]

$$g(r) = \left(a_0 r^{-2} + a_1 r^{-1} + a_2 + a_3 r + a_4 r^2 + a_5 r^3 \right) \cdot e^{-a_6 r}. \quad (3)$$

Fit parameters were calculated by the Carleton Laboratory for Radiotherapy Physics (CLRP) using the `egs_brachy` Monte Carlo software, as part of their AAPM Task Group No. 43 parameter database (for the AgX100 ^{125}I seed) [19].

Using (2) and (3), we can calculate the values for $G(r, \theta)$ and $g(r)$ at any nominal distance, and we can also calculate the influence of a ± 0.1 -mm shift at any nominal distance. Furthermore, since $G(r, \theta)$ and $g(r)$ are the two parameters, which influence the fall-off in the dose rate as a function of distance from the source (in this work), dividing normalized PCR measurement data by $G(r, \theta)/G(r_0, \theta_0)$, for example, should yield a result, which scales with $g(r)$ or vice versa. In this way, a comparison between theoretical expectation and measured PCR data can be performed.

III. RESULTS

Fig. 4 shows a relative comparison of the PCR fall-off along the transverse axis as a function of distance from the ^{125}I source, over the distance range of 5–30 mm, for each of the scintillator geometries considered in this work. The “expected” fall-off in the dose rate as a function of distance from the source is characterized by $G(r, \theta)$ and $g(r)$ as previously discussed. Dividing normalized data in Fig. 4 by the value for $G(r, \theta)/G(r_0, \theta_0)$ at each measurement distance yields the results shown in Fig. 6 for each scintillator geometry. Note that the error bars on the measurement data in Figs. 4–7 represent three times the standard error of the mean ($\sigma_{\bar{\mu}_i}$) measurement signal at each distance.

Fig. 5 shows the measured PCR, using a hemisphere tip geometry (1.0-mm-diameter core fiber), as a function of distance from the source. The DCR at the employed discriminator threshold voltage of -15 mV was ~ 63 kHz. The PCR signal

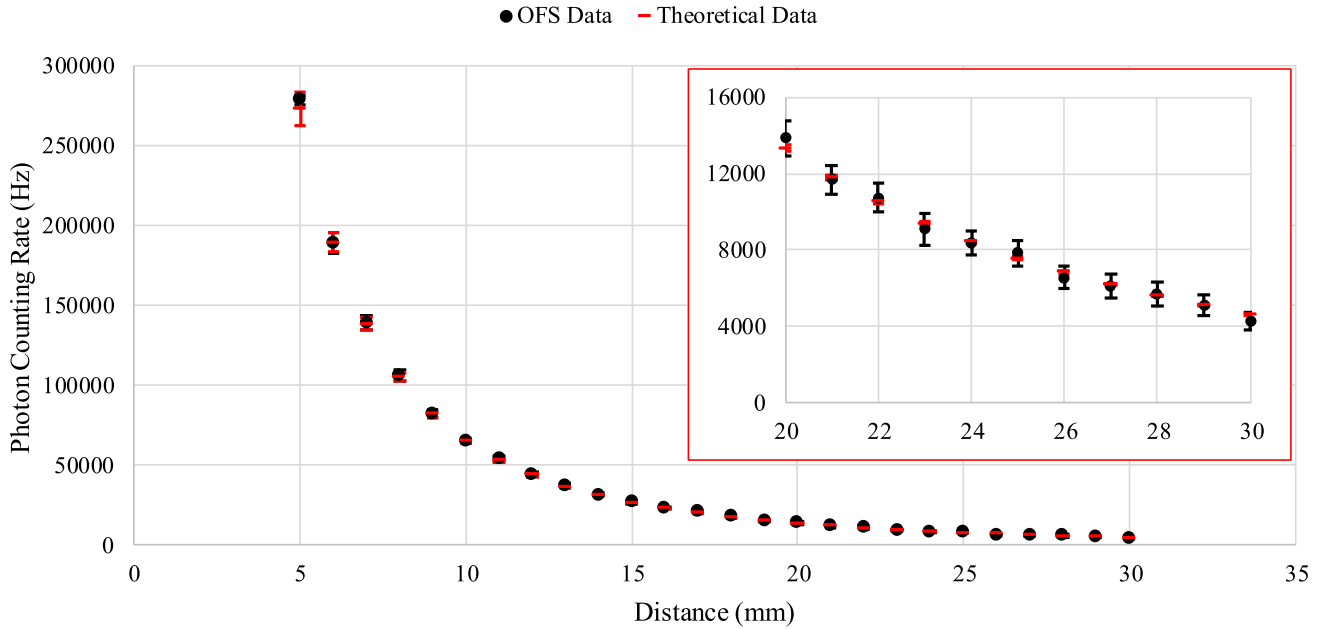


Fig. 5. PCR fall-off as a function of distance from the source (black circles), with a relative comparison (normalized to 10 mm) to the expected fall-off in dose rate (red dash). An inset of the data from 20 to 30 mm is included on the right-hand side of the graph, rescaled for clarity.

TABLE II

INFLUENCE OF FIBER CORE DIAMETER (\emptyset) AND SENSOR HOUSING MATERIAL ON SCINTILLATION SIGNAL

	0.5 mm \emptyset (Plastic) / 1.0 mm \emptyset (Plastic)	0.5 mm \emptyset (SS) / 1.0 mm \emptyset (Plastic)
Mean	0.166	0.072
Minimum	0.151	0.067
Maximum	0.177	0.078

5 mm from the source was ~ 279 kHz (in excess of the DCR), falling to ~ 4 kHz (in excess of the DCR) 30 mm from the source. Agreement with theoretical expectation [i.e., the product of $G(r, \theta)/G(r_0, \theta_0)$ and $g(r)$] is clearly evident, across the entire range of distances considered, within measurement uncertainty. Note that the error bars on the theoretical data represent the calculated impact of a ± 0.1 -mm shift at each distance.

The influence of moving from a 1.0-mm-diameter core fiber (in a plastic needle) to 0.5-mm-diameter core fiber (in plastic and stainless-steel needles) was also considered. Ratios of the measured PCRs (mean, minimum, and maximum) across the entire measurement range are provided in Table II. Moving from a 1.0-mm-diameter core fiber to 0.5-mm-diameter core fiber (both in plastic needles) results in an approximate sixfold reduction in the PCR. A further $\sim 57\%$ reduction in the PCR is observed when housing the 0.5-mm-diameter fiber in a stainless steel LDR BT needle applicator. It is worth noting that a hemisphere tip geometry (diameter 1.0 mm) was employed for both the 1.0-mm fiber core diameter and the 0.5-mm fiber core diameter and that the DCR remained at ~ 63 kHz

for the three datasets shown. Normalizing the measurement data and dividing by the value for $G(r, \theta)/G(r_0, \theta_0)$ at each measurement distance yields the results provided in Fig. 7, for each fiber diameter/needle configuration considered.

IV. DISCUSSION

Water phantom measurements presented in this work were obtained over the clinically relevant distance range of 5–30 mm. The minimum distance of 5 mm was chosen since this distance describes the spacing on the LDR BT template grid. The maximum distance of 30 mm was chosen based on average dimensions of the prostate gland of ~ 60 mm, as obtained from an in-house clinical audit. Assuming a distribution of sensor locations within the prostate and indeed within the urethra, sensitivity over a range of 30 mm was deemed sufficient to ensure coverage of the entire prostate.

Considering Fig. 4, differences in the relative response for each of the scintillator geometries considered are observed. A relative comparison was performed since each of the sensors considered in this work was fabricated manually. Therefore, differences in the raw scintillation signal generated by each sensor may be observed, which are not due to the scintillator geometry employed. For example, slight variations in the FC connection from one sensor to the next, the use of pure scintillator powder in the cylindrical cavities versus a powder-NOA 61 epoxy mix in the hemisphere tip, the distribution of dopant sites within the scintillator volume, and so on. However, the relative change in the response as a function of distance from the source should be independent of the raw scintillation signal and in this way should allow for a comparison of the scintillator geometries considered. The observed differences in Fig. 4 are particularly evident when the normalized data are divided by $G(r, \theta)/G(r_0, \theta_0)$ and compared to $g(r)$, as shown in Fig. 6. The hemisphere

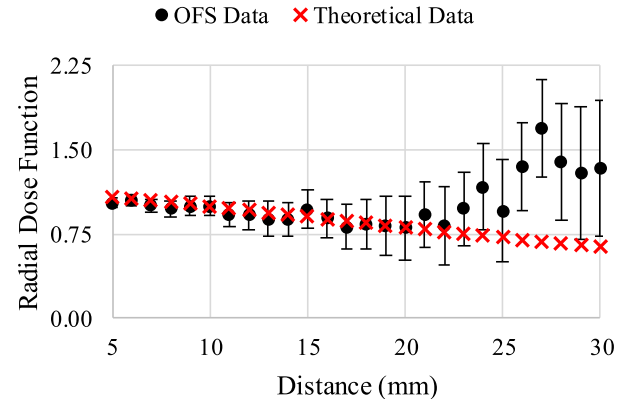
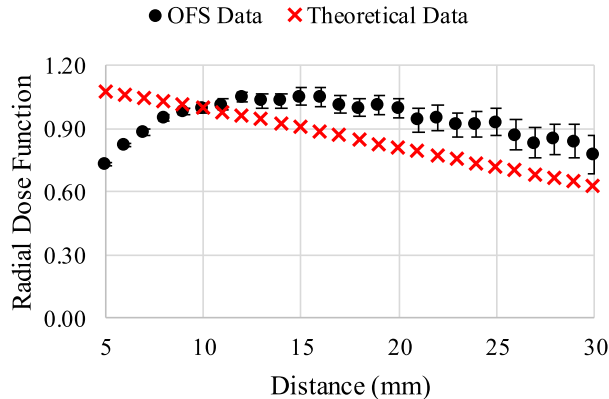
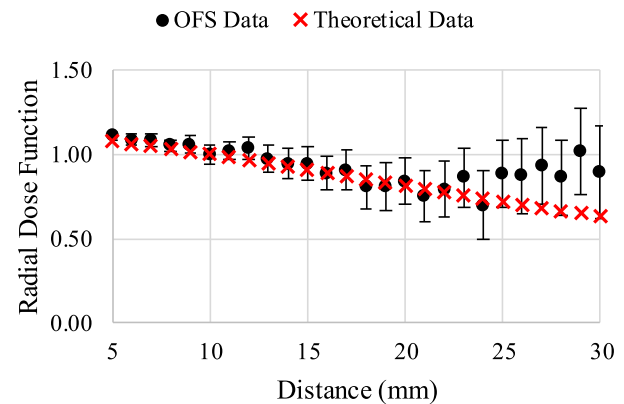
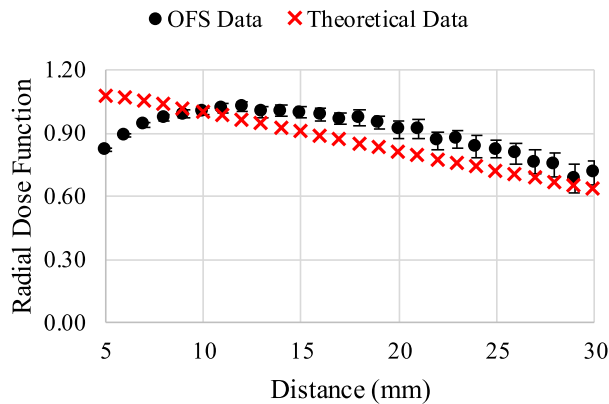
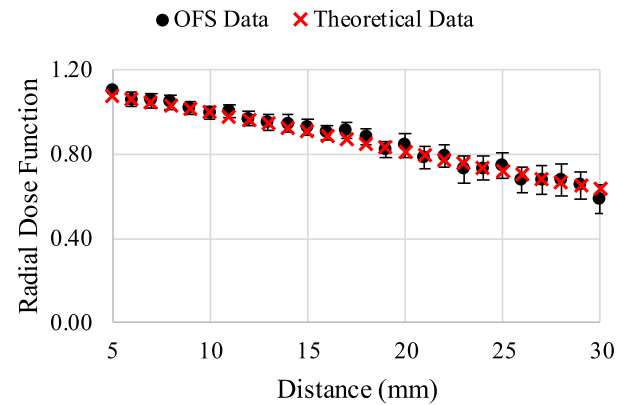
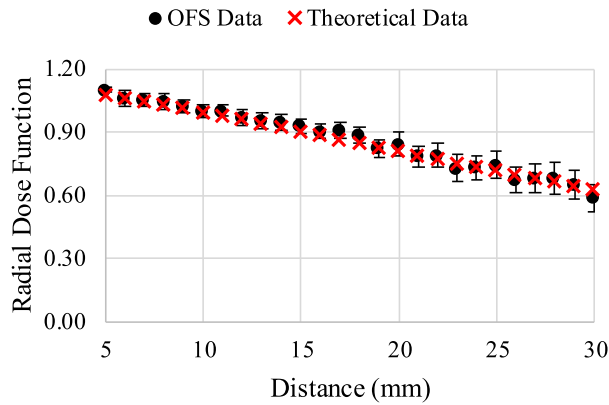


Fig. 6. Comparison of the radial dose function, based on OFS data (black circles) and theoretical data (red crosses), for (top) hemisphere tip, (middle) 5-mm deep cylindrical cavity, and (bottom) 7-mm deep cylindrical cavity.

Fig. 7. Comparison of the radial dose function, based on OFS data (black circles) and theoretical data (red crosses), for (top) 1.0-mm fiber in a plastic needle and (middle) 0.5-mm fiber in plastic and (bottom) stainless steel needles.

tip geometry provides the best agreement with theoretical expectation, agreeing with $g(r)$ within uncertainty. For both of the cylindrical cavity geometries considered, a relative under-response is observed at distances closer than 10 mm (normalization distance) from the ^{125}I source, while an over-response is observed at distances greater than 10 mm. It is also noted that the observed deviation from theoretical expectation increases with increasing depth of the cavity. This finding can, in part, be explained by the steep dose gradient around the ^{125}I source, that is to say, due to variation in the dose rate to the scintillator across its length, theoretical data (calculations)

may need to be integrated over the length of the scintillator, as previously described by Theriault-Proulx et al. [11] for their 5-mm-long plastic scintillation detector. However, there is an additional consideration for inorganic scintillation detectors (such as $\text{Gd}_2\text{O}_2\text{S:Tb}$); the scintillator material is not transparent with respect to the scintillation light it produces. Therefore, as you move along the cylindrical volume of the cavity (away from fiber), less scintillation light is coupled into the fiber, reducing the light collection efficiency [20]. Furthermore, for the cavity geometries considered, although they are cylindrically symmetrical, eliminating any angular

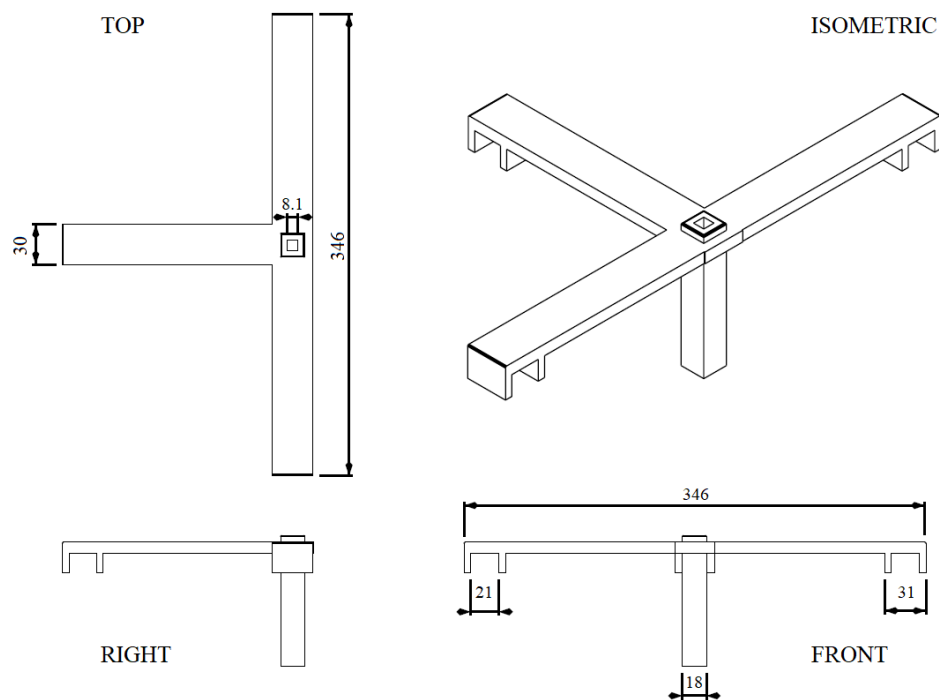


Fig. 8. Schematic of the 3-D printed T-junction top support for the source holder (unit: mm), from multiple views.

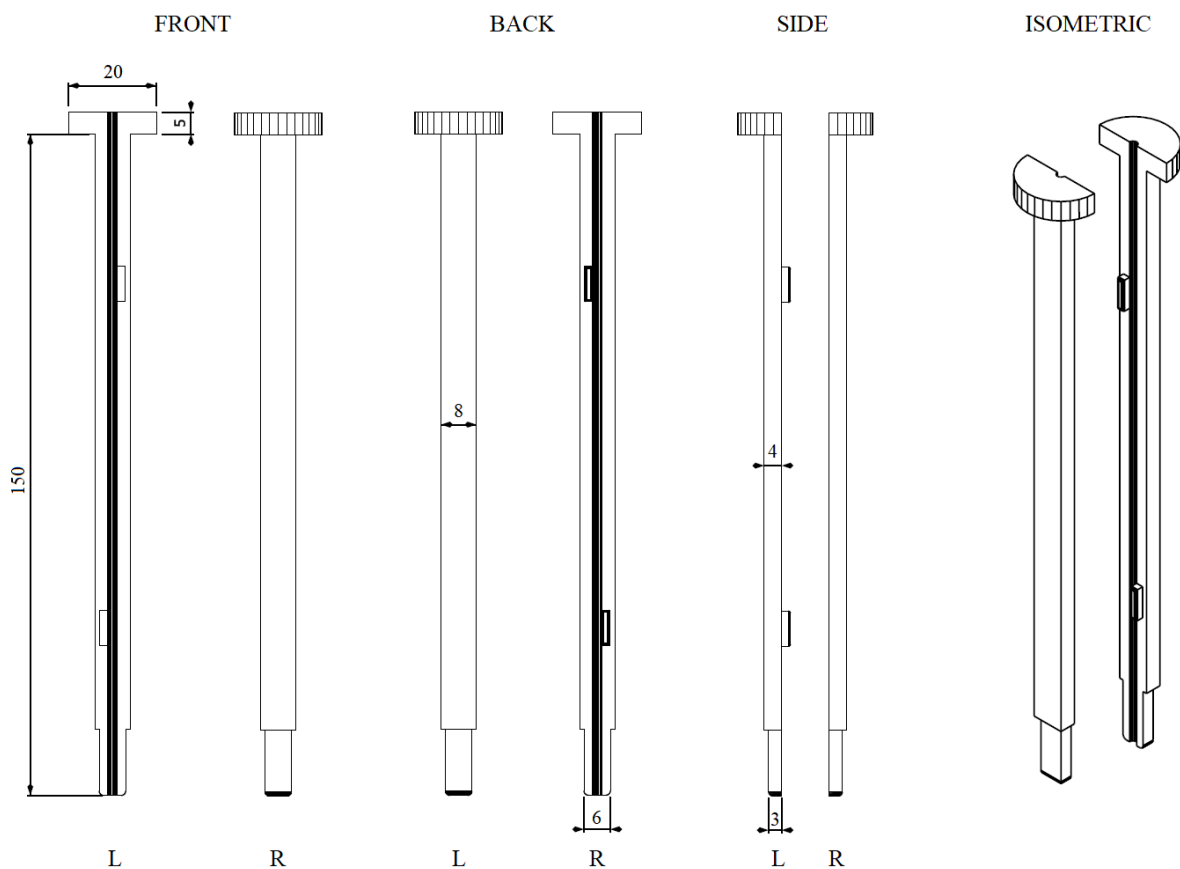


Fig. 9. Schematic of the 3-D printed source holder (unit: mm), from multiple views. This component is printed in two parts, left (L) and right (R). The central channel is matched in diameter to that of the BT needle that holds the source.

dependence for the measurements performed in this work, they are likely to exhibit an angular dependence in the longitudinal plane [20], which could possibly limit future use as an in vivo dosimeter. Based on these findings, it was decided to focus on

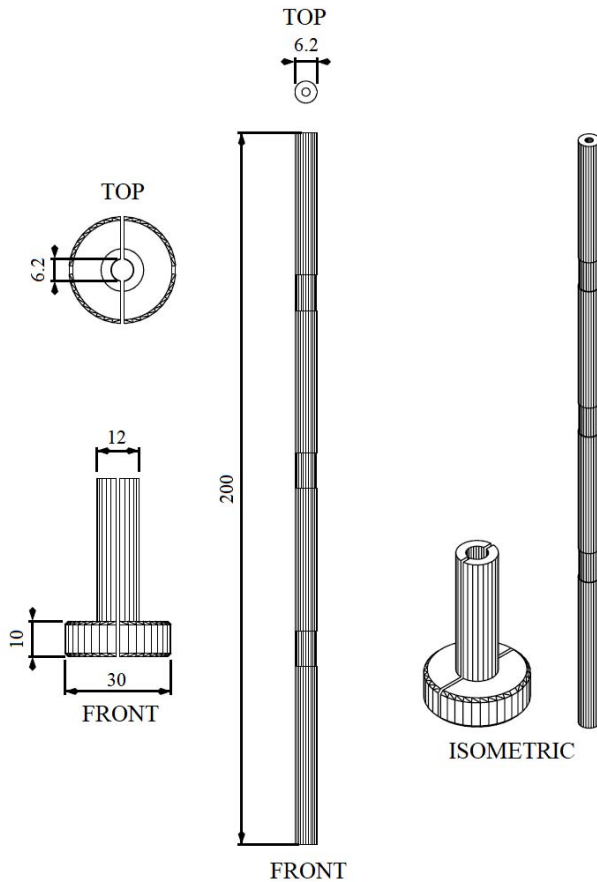


Fig. 10. Schematic of the 3-D printed OFS holder (unit: mm), from multiple views. Two distinct components are shown: 1) the component that slots into the Markus Chamber holder and 2) the cylindrical “guide tube” that is delivered through 1) and constrains the position of the sensor in a parallel orientation. Note: central channel of 2) is matched in diameter to that of the BT needle that holds the sensor.

the hemisphere tip scintillator geometry for the remainder of this work.

Referring to Fig. 5, agreement between measured PCR data and theoretical expectation, within uncertainty, is evident across the 5–30-mm distance range. This finding indicates that an “energy correction” to account for changes in the response of the sensor as a function of distance from the source, due to changes in the energy spectra and the high-density nontissue equivalent inorganic scintillator material, may not be required for applications in LDR prostate BT. Furthermore, previous Monte Carlo modeling studies have independently reported that changes in the energy spectra of ^{125}I with distance are small, particularly over the distance range considered in this work [21], [22]. Based on these findings, we believe that the conversion from PCR to absorbed dose will require only a single calibration coefficient. Calculation of this calibration coefficient could be achieved in the water phantom using an AgX100 ^{125}I seed “calibrated” by performing a measurement using a radiation dosimeter with a traceable calibration to a “primary standard.” The PCR could be measured at a reference

distance of 10 mm from the source on the transverse axis, in the water phantom; using the known dose rate from the calibrated seed, a calibration coefficient could be calculated with units of absorbed dose per unit frequency (e.g., cGy/kHz). A distance of 10 mm from the ^{125}I source for the purposes of calibration strikes a balance between the influence of the positional and noise components of the measurement uncertainty. It is also consistent with the definition of the “reference position” from the AAPM Task Group No. 43 Report [16], [17], defined as lying on the transverse bisector of the source at a distance of 1 cm.

The influence of the fiber core diameter on the measured PCR was also considered, with a sixfold reduction observed for the 0.5-mm fiber core compared to the 1.0-mm fiber core, when both are housed within a plastic needle. Taking the 0.5-mm fiber core and then placing it within the clinically relevant stainless steel LDR BT needle applicator resulted in a further $\sim 57\%$ reduction in the PCR, due to attenuation of the low-energy photons associated with ^{125}I (maximum energy ~ 35.5 keV). A result of the observed reduction in the scintillation signal for the 0.5-mm fiber core diameter was a relative increase in the magnitude of the noise component of the uncertainty (error bars), as shown in Fig. 7. This is due to the fluctuations in the DCR dominating the fluctuations in the measurement signal (DCR + PCR), as the PCR reduces. There is the additional possibility for transient fluctuations in the measurement signal to negatively impact measurement accuracy, particularly as the PCR reduces. It is worth highlighting, however, that the data obtained using the 0.5-mm fiber core diameter, shown in Fig. 7, remained in agreement with theoretical expectations within uncertainty, for distances of less than or equal to ≈ 25 mm. The observed reductions in PCR may necessitate the use of larger integration times during data acquisition, to achieve acceptable levels of statistical uncertainty. Future work could investigate if further optimization of the scintillator geometry, optical coupling, and/or SiPM characteristics (e.g., thermo-electric cooling) could be employed to offset the observed reductions in PCR.

These results indicate that the rate of fall-off in the PCR is dependent on the characteristics of the radiation source and the geometry of the scintillator (see Figs. 4 and 6). The use of the 0.5-mm fiber would have the advantage of allowing more fibers to occupy the same space (e.g., within a needle/catheter) and it would also allow for jacketed fibers to be inserted into the needle applicator, which would reduce the impact of ambient or parasitic light during a clinical procedure. Data obtained in this work demonstrate that the experimental design employed, including the water phantom system and 3-D printed components, has the potential to be employed for the characterization and calibration of OFSs, within different BT needles/applicators.

V. CONCLUSION

A custom water-phantom system-based experimental design is presented in this work and employed to obtain precise OFS measurements, for applications in LDR prostate BT. Results

obtained demonstrate that the rate at which the scintillation signal falls off with distance from the clinical radiation source ($\text{AgX100 }^{125}\text{I}$ seed), specifically for the hemisphere tip geometry, agrees with theoretical expectation for the fall-off in dose rate. Furthermore, water phantom measurements indicate that an “energy correction” to account for both changes in the energy spectra as a function of distance from the radiation source and the high-density nontissue equivalent inorganic scintillator material may not be required for applications in LDR prostate BT. Based on these findings, we believe that the conversion from scintillation signal to absorbed dose requires only a single calibration coefficient, and a calibration process has been described. The influence of employing a 0.5-mm-diameter fiber on the scintillation signal was also considered, with and without incorporating a clinically relevant LDR BT stainless steel needle applicator. While these configurations pose challenges due to the reduced signal, initial results demonstrate that they are feasible, given the continued agreement with theoretical expectations.

APPENDIX

See Figs. 8–10.

ACKNOWLEDGMENT

The ORIGIN Project is an initiative of the Photonics Public Private Partnership (www.photonics21.org).

REFERENCES

- [1] E. Rosenblatt, O. Acuña, and M. Abdel-Wahab, “The challenge of global radiation therapy: An IAEA perspective,” *Int. J. Radiat. Oncol.*Biol.*Phys.*, vol. 91, no. 4, pp. 687–689, Mar. 2015, doi: [10.1016/j.ijrobp.2014.12.008](https://doi.org/10.1016/j.ijrobp.2014.12.008).
- [2] R. Baskar, K. A. Lee, R. Yeo, and K. W. Yeoh, “Cancer and radiation therapy: Current advances and future directions,” *Int. J. Med. Sci.*, vol. 9, no. 3, pp. 193–199, Feb. 2012, doi: [10.7150/ijms.3635](https://doi.org/10.7150/ijms.3635).
- [3] H. Gelband, P. Jha, R. Sankaranarayanan, and S. Horton, Eds., *Disease Control Priorities: Cancer*, vol. 3, 3rd ed., Nov. 2015, doi: [10.1596/978-1-4648-0349-9](https://doi.org/10.1596/978-1-4648-0349-9).
- [4] B. Podgoršak, *Radiation Oncology Physics: A Handbook for Teachers and Students*. Vienna, Austria: International Atomic Energy Agency, 2005, p. 454.
- [5] R. G. Stock, N. N. Stone, M. F. Wesson, and J. K. DeWynngaert, “A modified technique allowing interactive ultrasound-guided three-dimensional transperineal prostate implantation,” *Int. J. Radiat. Oncol.*Biol.*Phys.*, vol. 32, no. 1, pp. 219–225, Apr. 1995, doi: [10.1016/0360-3016\(95\)00521-y](https://doi.org/10.1016/0360-3016(95)00521-y).
- [6] R. Stock, N. Stone, A. Tabert, C. Iannuzzi, and J. Dewynngaert, “A dose-response study for I-125 prostate implants,” *Int. J. Radiat. Oncol.*Biol.*Phys.*, vol. 41, no. 1, pp. 101–108, Apr. 1998, doi: [10.1016/s0360-3016\(98\)00006-6](https://doi.org/10.1016/s0360-3016(98)00006-6).
- [7] A. Polo, C. Salembier, J. Venselaar, and P. Hoskin, “Review of intraoperative imaging and planning techniques in permanent seed prostate brachytherapy,” *Radiotherapy Oncol.*, vol. 94, no. 1, pp. 12–23, Jan. 2010, doi: [10.1016/j.radonc.2009.12.012](https://doi.org/10.1016/j.radonc.2009.12.012).
- [8] T. P. Hellebust, “Place of modern imaging in brachytherapy planning,” *Cancer/Radiothérapie*, vol. 22, no. 4, pp. 326–333, Jun. 2018, doi: [10.1016/j.canrad.2018.03.005](https://doi.org/10.1016/j.canrad.2018.03.005).
- [9] A. P. Brown et al., “Improving prostate brachytherapy quality assurance with MRI-CT fusion-based sector analysis in a phase II prospective trial of men with intermediate-risk prostate cancer,” *Brachytherapy*, vol. 12, no. 5, pp. 401–407, Sep. 2013, doi: [10.1016/j.brachy.2012.10.001](https://doi.org/10.1016/j.brachy.2012.10.001).
- [10] P. Woulfe et al., “Optical fibre based real-time measurements during an LDR prostate brachytherapy implant simulation: Using a 3D printed anthropomorphic phantom,” *Sci. Rep.*, vol. 11, no. 1, pp. 1–8, May 2021, doi: [10.1038/s41598-021-90880-6](https://doi.org/10.1038/s41598-021-90880-6).
- [11] F. Therriault-Proulx, L. Beaulieu, and S. Beddar, “Validation of plastic scintillation detectors for applications in low-dose-rate brachytherapy,” *Brachytherapy*, vol. 16, no. 4, pp. 903–909, Jul. 2017, doi: [10.1016/j.brachy.2017.04.002](https://doi.org/10.1016/j.brachy.2017.04.002).
- [12] *X-Ray Phosphors*. Phosphor Technology Ltd. Accessed: Oct. 5, 2022. [Online]. Available: <https://www.phosphor-technology.com/x-ray-phosphors/>
- [13] E. I. Gorokhova, V. A. Demidenko, S. B. Mikhlin, P. A. Rodnyi, and C. W. E. van Eijk, “luminescence and scintillation properties of $\text{gd}_2\text{o}_2\text{S}:\text{Tb,Ce}$ ceramics,” *IEEE Trans. Nucl. Sci.*, vol. 52, no. 6, pp. 3129–3132, Dec. 2005, doi: [10.1109/tns.2005.862827](https://doi.org/10.1109/tns.2005.862827).
- [14] (2019). *Solutions Radiation Medicine QA*. Accessed: Oct. 5, 2022. [Online]. Available: <https://www.ptwdosimetry.com/en/products/pqasoft/?type=3451&downloadfile=1816&cHash=db2ab6cad43c81fd0f77e08bdd60f0f9>
- [15] C. Mattone et al., “CAEN educational: Nuclear and particle physics experiments,” in *Proc. Conf. Lab. Instruct. Beyond First Year College*, Jul. 2018, pp. 1–4, doi: [10.1119/bfy.2018.pr.011](https://doi.org/10.1119/bfy.2018.pr.011).
- [16] R. Nath, L. L. Anderson, G. Luxton, K. A. Weaver, J. F. Williamson, and A. S. Meigooni, “Dosimetry of interstitial brachytherapy sources: Recommendations of the AAPM radiation therapy committee task group, no. 43,” *Med. Phys.*, vol. 22, no. 2, pp. 209–234, Feb. 1995, doi: [10.1118/1.597458](https://doi.org/10.1118/1.597458).
- [17] M. J. Rivard et al., “Update of the AAPM task group, no. 43 report—A revised AAPM protocol for brachytherapy dose calculations,” *Int. J. Radiat. Oncol.*Biol.*Phys.*, vol. 57, no. 2, p. S430, Oct. 2003, doi: [10.1016/s0360-3016\(03\)01389-0](https://doi.org/10.1016/s0360-3016(03)01389-0).
- [18] R. E. P. Taylor and D. W. O. Rogers, “More accurate fitting of I125 and Pd103 radial dose functions,” *Med. Phys.*, vol. 35, no. 9, pp. 4242–4250, Aug. 2008, doi: [10.1118/1.2964097](https://doi.org/10.1118/1.2964097).
- [19] H. Safigholi et al., “Update of the CLRP TG-43 parameter database for low-energy brachytherapy sources,” *Med. Phys.*, vol. 47, no. 9, pp. 4656–4669, Jul. 2020, doi: [10.1002/mp.14249](https://doi.org/10.1002/mp.14249).
- [20] S. Beddar and L. Beaulieu, Eds., *Scintillation Dosimetry*, Sep. 2018, pp. 156–158, doi: [10.1201/9781315372655](https://doi.org/10.1201/9781315372655).
- [21] A. S. Meigooni, J. A. Meli, and R. Nath, “A comparison of solid phantoms with water for dosimetry of ^{125}I brachytherapy sources,” *Med. Phys.*, vol. 15, no. 5, pp. 695–701, Sep. 1988, doi: [10.1118/1.596182](https://doi.org/10.1118/1.596182).
- [22] K. A. Weaver, V. Smith, D. Huang, C. Barnett, M. C. Schell, and C. Ling, “Dose parameters of ^{125}I and ^{192}Ir seed sources,” *Med. Phys.*, vol. 16, no. 4, pp. 636–643, Jul. 1989, doi: [10.1118/1.596322](https://doi.org/10.1118/1.596322).



Michael Martyn (Member, IEEE) received the B.Sc. (Hons.) degree in physics with medical physics and the M.Sc. and structured Ph.D. degrees in medical physics from the University of Galway, Galway, Ireland, in 2011, 2012, and 2018, respectively.

His Ph.D. study was focused on the applications of ultrasound imaging in radiotherapy, particularly in the treatment of prostate cancer and quantification of the dosimetric effects with Monte Carlo techniques. Upon completion of his

Ph.D. degree in 2018, he worked as a Clinical Medical Physicist at University Hospital Galway, Galway, as part of the Radiotherapy Physics Team. In August 2020, he took up a role as a Research Medical Physicist at the Blackrock Health Galway Clinic, Galway, working on the Horizon 2020 funded ORIGIN Project. This work focuses on the development of optical fiber-based dose imaging techniques for applications in adaptive brachytherapy. In June 2021, he also took up a role as an Adjunct Lecturer in Medical Physics at the University of Galway.

Dr. Martyn is a Professional Member of the Irish Association of Physicists in Medicine and a member of the Society of Photo-Optical Instrumentation Engineers.



Wern Kam (Member, IEEE) received the B.Sc. and M.Sc. degrees in physics from the University of Malaya, Kuala Lumpur, Malaysia, in 2012 and 2015, respectively, and the Ph.D. degree in electronic and computer engineering from the University of Limerick, Limerick, Ireland, in 2018, funded by the Erasmus Mundus LEADERS.

Through her doctoral research, she has developed a 3-D printed plastic optical fiber-based sensor for monitoring spine bending and respiratory signal for measurements in the clinical environment. She was a Postdoctoral Researcher with the Optical Fiber Sensors Research Centre (OFSRC), University of Limerick, developing optical fiber sensor systems for radiation dose monitoring during brachytherapy procedures. Her research interests include fiber optic sensors, wearable devices, and medical sensors.



Peter Woulfe (Member, IEEE) received the M.Sc. degree in medical physics from the University of Galway, Galway, Ireland, in 2003, where his thesis was focused on the development of a novel chest phantom for digital radiography. He is currently pursuing the Ph.D. degree from the Optical Fiber Sensor Research Centre (OFSRC), University of Limerick, Limerick, Ireland, developing radiation dosimeters for monitoring patient doses received during radiotherapy for cancer treatment.

On completion of his M.Sc. degree, he took up a role at the National Centre for Laser Applications (NCLA), University of Galway, which led him to his current role as a Radiotherapy Medical Physicist with the Blackrock Health Galway Clinic, Galway, progressing from a Trainee Physicist in 2004 to a Medical Physicist Expert in 2009, and currently the Chief Medical Physicist leading a team of eight Physicists in the Clinic.

Mr. Woulfe's professional affiliations include a membership of the Irish Association of Physicists in Medicine and the Institute of Physics and Engineering in Medicine and a Full Membership of the Irish College of Physicists in Medicine. He is also registered as a Chartered Scientist in U.K. and with the Health and Care Professions Council in U.K.



Sinead O'Keeffe (Member, IEEE) received the B.E. (Hons.) degree in electronic engineering and the Ph.D. degree, for the development of polymer optical fiber sensors for the sterilization industry, from the University of Limerick, Limerick, Ireland, in 2003 and 2006, respectively.

On completion of her Ph.D. degree, she has worked as a Marie Curie Research Fellow with the General Engineering Research Institute, Liverpool John Moores University, Liverpool, U.K., developing optical fiber sensors for monitoring ultraviolet (UV) and ozone. She returned to the Optical Fiber Sensors Research Centre, University of Limerick, in 2008, where she received the FP7 Marie Curie Research Fellowship, developing radiation dosimeters for monitoring patient doses received during radiotherapy for cancer treatment. She is currently a Royal Society–Science Foundation Ireland University Research Fellow at the University of Limerick, leading a team that focuses on the development of optical fiber-based sensor systems for the diagnosis, assessment, and treatment of cancer tumors. She is also a coordinator of the European H2020 Project “ORIGIN,” developing optical fiber-based sensors for real-time dose imaging and source localization for adaptive brachytherapy.

Dr. O'Keeffe was a Member-at-Large of the IEEE Sensors Council from 2017 to 2020. She is the Chair of the IEEE Sensors Council Diversity and Inclusion Committee for the term 2020–2022.